Performance of Different ANNs in Microtremor H/V Peak Classification

Published Version:
Di Donato, M., Castellaro, S. (2024). Performance of Different ANNs in Microtremor H/V Peak Classification. SEISMOLOGICAL RESEARCH LETTERS, 95(6), 3722-3736 [10.1785/0220230258].

Availability:
This version is available at: https://hdl.handle.net/11585/1013283 since: 2025-03-31

Published:
DOI: http://doi.org/10.1785/0220230258

Performance of different ANNs in microtremor H/V peak classification

Miriana Di Donato[1*], Silvia Castellaro[1]

[1] Dipartimento di Fisica e Astronomia, Alma Mater Studiorum Università di Bologna, viale C. B. Pichat 8, Italy

*[corresponding author] miriana.didonato3@unibo.it, silvia.castellaro@unibo.it

Abstract

The microtremor H/V technique is extensively used to both assess the seismic amplification potential of soils, and, often in combination with other surface wave-based techniques, to reconstruct the near surface seismic stratigraphy. The H/V peak frequencies are traditionally interpreted in terms of soil resonances, and, in this case, they are assigned a 'stratigraphic origin'. However, not all H/V peaks mark subsoils resonances and some of them has 'anthropic' or 'artefactual' origin. Recognizing the nature of H/V peaks should be mandatory before any stratigraphic interpretation. Nonetheless, this problem is not given the attention it deserves. As this classification is not easy to achieve by means of standard statistical techniques, we decided to train two supervised neural networks: a traditional Artificial Neural Network using a set of input values extracted from the individual (horizontal and vertical) microtremor spectra, and a Convolutional Neural Network, working on images of the microtremor spectra. The nets were trained on an Italian dataset and tested on a US dataset, collected by different operators and with different instruments. Both nets achieved a classification accuracy of approximately 90%; however, the convolutional one showed a greater generalization capability compared to the traditional one. Such machine learning algorithms can be useful tools to discriminate the origin of H/V peaks, complementing the traditional SESAME guidelines, which do not go into much detail on this topic.

Key-words: H/V, artefactual H/V peaks, artificial neural network, convolutional neural network

Introduction

Artificial neural networks, introduced for the first time in 1943 by Warren McCulloch and Walter Pitts, landed in applied geophysics in the late 1980s. Recent applications of artificial neural networks in geophysics include, e.g., the prediction of site amplification response (Bergamo et al., 2021; Boudghene Stambouli et al., 2017; Salameh et al., 2017) and seismic site classification related issues (Zhao, 2006; Ghasemi et al., 2009; Yaghmaei-Sabegh & Tsang, 2011; Ji et al., 2022; Díaz et al., 2022; Vantassel et al., 2023).

In this paper we focus on microtremor H/V curves. The identification of significant peaks therein is traditionally assessed by means of the SESAME (2004) criteria, which, however, cannot discriminate between the stratigraphic and non-stratigraphic (anthropogenic or artefactual) nature of them. SESAME (2004), states that *''if the microtremor spectra components exhibit a sharp peak (often on the 3 components together), at*

a particular frequency, there is a 95% chance that this is anthropic "forced" ambient vibration and it should not be considered in the interpretation''. However, the SESAME (2004) criteria do not provide specific rules to reject these artefacts.
Recently, Wang et al. (2023) proposed an identification protocol for H/V peaks based on a regression tree algorithm. This algorithm, however, does not even consider that H/V peaks can have stratigraphic or non-stratigraphic origins and that their shape is very different in the two cases.

Non-stratigraphic spectral peaks are typically caused by machineries acting in the proximity of the recording station (e.g. wind-mills, industrial machines; Dreossi et al., 2018) or result as an effect of vibrations induced from large nearby structures (tall buildings and bridges or viaducts; Castellaro & Mulargia, 2010; Castellaro et al., 2022). Low frequency (i.e., large wavelength) artefacts can perturb the noise wavefield up to very large distances from the source. They have been documented up to even a few km distance from their source (Bokelmann & Baisch, 1999; Cornou et al., 2004, Dreossi et al., 2018).
The frequency of anthropogenic peaks can also potentially coincide with the frequency of stratigraphic peaks.

H/V curves are not infrequently affected by artefactual peaks, and it is mandatory to discriminate them, before attempting any interpretation of the H/V curves themselves. This is a relevant issue if one considers the worldwide extended use of the H/V technique in seismic microzonation, in seismic soil classification (where it is commonly combined with surface wave multichannel methods to get Vs profiles) and in the classification of soils around seismic stations, which influence the signal recorded by them.
The H/V curves produced by automatic processing of 3C-microtremor recordings from permanent seismic stations would also require automatic algorithms for real-time or off-line identification of non-stratigraphic peaks.

Given the limited capability of standard statistical techniques in this type of signal classification, due to the strong variability of the geometries of non-stratigraphic H/V peaks, we decided to explore the performance of different artificial neural networks in discriminating between stratigraphic and non-stratigraphic features in microtremor signals.
In the following sections, we first present the features distinguishing stratigraphic from non-stratigraphic H/V peaks, then we illustrate the two types of neural networks trained to this aim, the performance of both and their limitations.

Stratigraphic vs. non-stratigraphic H/V peaks

Microtremor H/V peaks can be due to the presence of local maxima (peaks) in the horizontal spectral components of motion, to the presence of local minima (troughs) in the vertical component of motion or to the occurrence of both conditions, with different amplitudes.

Peaks in the horizontal components of motion (Figure 1a, b) are typically associated with body wave resonances (e.g., Nakamura, 1989; Van Der Baan, 2009; Castellaro, 2016; Oubaiche et al., 2016; Molnar et al., 2018; Sgattoni & Castellaro, 2020; Molnar et al., 2022; Castellaro & Musinu, 2023). Troughs in the vertical spectral component motion (Figure 1c, d), occurring at or close to the resonance frequency of SH waves, f_0, are instead typical of surface wave trapping phenomena (Fäh et al., 2001; Bonnefoy-Claudet et al., 2008; Castellaro & Mulargia, 2009a; Endrun, 2011; Tuan et al., 2011; Castellaro, 2016; Molnar et al., 2022).
A local maximum in the vertical spectral component follows at about twice the frequency of the trough (Konno & Ohmachi, 1998; Fäh et al., 2001; Tuan et al., 2011; Castellaro, 2016).
Thus, the H/V curves typically exhibit a peak at the frequency of the vertical trough f_0 and the H/V ratio returns to its non-amplified value (H/V $\sim$ 1) at about $2f_0$ (Figure 1, Tuan et al., 2011; Castellaro, 2016).

Another distinctive feature of H/V curves acquired in 1D conditions is that the horizontal components are statistically identical through the whole frequency spectrum as clear in Figure 1. Outside the H/V peak frequency interval, the horizontal and vertical spectra are again statistically identical in amplitude (thus, H/V$\sim$1).
For the meaning of H/V < 1 in wide frequency intervals and for more examples, see, e.g., Castellaro & Mulargia (2009b).

H/V peaks with marked troughs in the vertical component dominate in 1D conditions and in low aspect ratio basins while H/V peaks dominated by local maxima in the horizontal components of motion are typical in markedly 2-3D conditions, like large aspect ratio basins (Bard & Bouchon, 1980a; Roten et al., 2006; Le Roux et al., 2012; Ermert et al., 2014; Sgattoni & Castellaro, 2020; Lattanzi et al., 2023; Sgattoni et al., 2023).

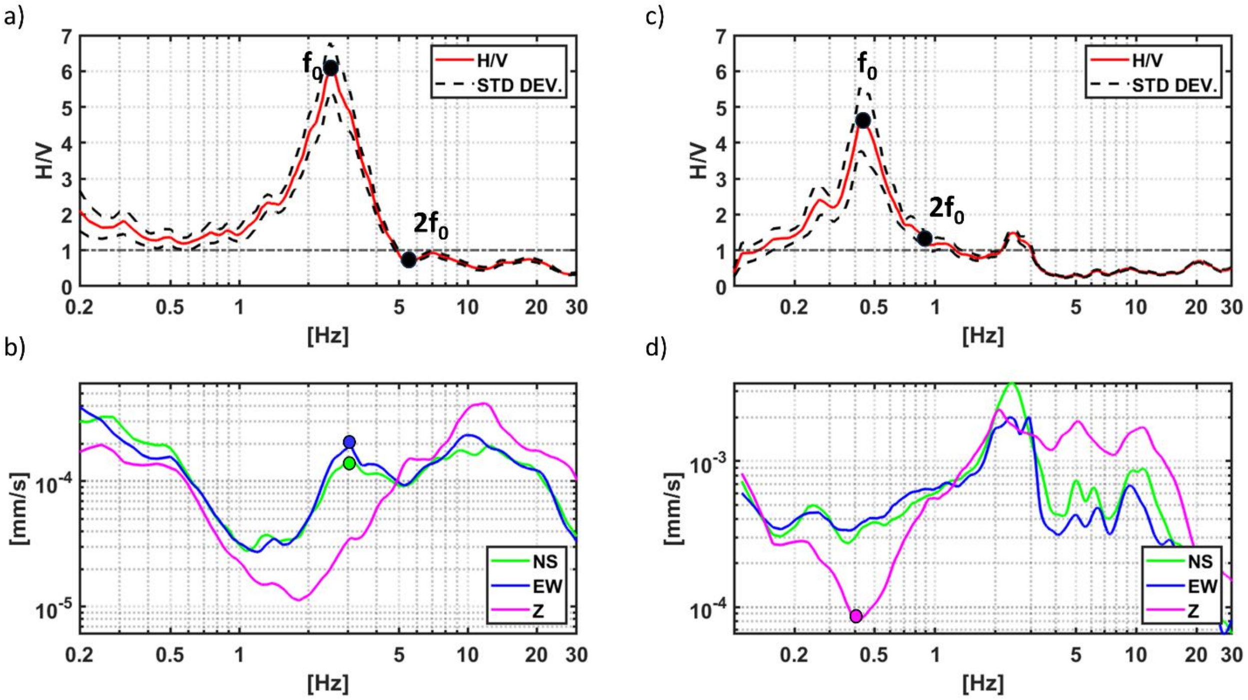

Figure 1. H/V peaks of stratigraphic origin: a, c) H/V curves and b, d) corresponding individual spectra of motion in velocity. Stratigraphic peaks occurring at f_0 typically 'close' around $2f_0$ (with a variability depending on the Poisson's ratio, Tuan et al., 2011). Here the H/V peaks are observed at $f_0 = 0.65\ Hz$ (a) and $f_0 = 1\ Hz$ (b) and the H/V curve turns back to H/V ~ 1 at $\sim 2f_0$ = 1.3 Hz and 2 Hz, respectively. The stratigraphic origin is marked by a local minimum in the vertical spectral component (more evident in panel d) and/or local maxima in the horizontal spectral component (more evident in panel b).

The SESAME (2004) guidelines introduced quantitative criteria to assess the reliability and clarity of peaks in H/V curves. These criteria were mostly based on the statistical analysis of the frequency and amplitude peak stability over time and on the expected geometrical shape for H/V peaks. No other rules were present in the SESAME criteria to discriminate between stratigraphic and non-stratigraphic peaks, beyond the general comment presented in the introduction.

Non-stratigraphic H/V peaks are typically generated by narrow spikes (almost Dirac's deltas, when non-smoothed) visible, with different amplitudes, on all spectral components (Figure 2). Comparing the smoothed (Figure 2b) and non-smoothed (Figure 2c) spectra makes the acknowledgement of artefactual peaks generally straightforward (Castellaro & Mulargia, 2010).

A non-stratigraphic H/V peak at frequency f_0 does not return to H/V ~ 1 at $2f_0$ but well before this value.

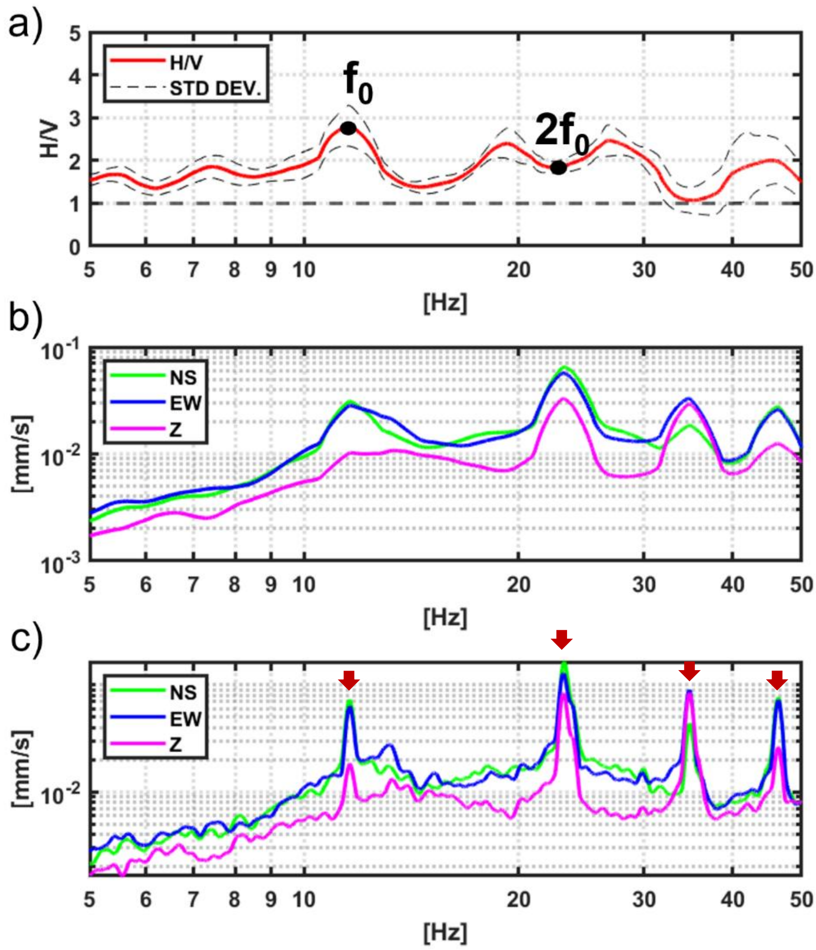

Figure 2. Non-stratigraphic H/V peaks (at 12 Hz, 24 Hz, 34 Hz, 46 Hz) induced by industrial machineries (marble sawmills) at a few hundred meters distance: a) H/V curve and b) corresponding amplitude spectra of the three components of motion with a 10% (of the central frequency) smoothing. c) is as b) but non-smoothed. The spectral peaks are very sharp in this case and have different amplitudes in the different components. This produces artefactual peaks and troughs in the H/V curve, where the distance between the H/V peaks and the return to H/V ~1 is much smaller than $[f_0, 2f_0]$ *in all cases.*

Other types of non-stratigraphic H/V peaks are those induced by the vibration of large nearby structures or infrastructures (e.g., bridges). They have the same features already discussed for Figure 2, but they typically occur at different frequencies along different axes, depending on the shape of the vibrating structures. These can be detected also by means of azimuthal processing (see e.g., Matsushima et al., 2014; Cheng et al., 2020). An example is given in Figure 3.

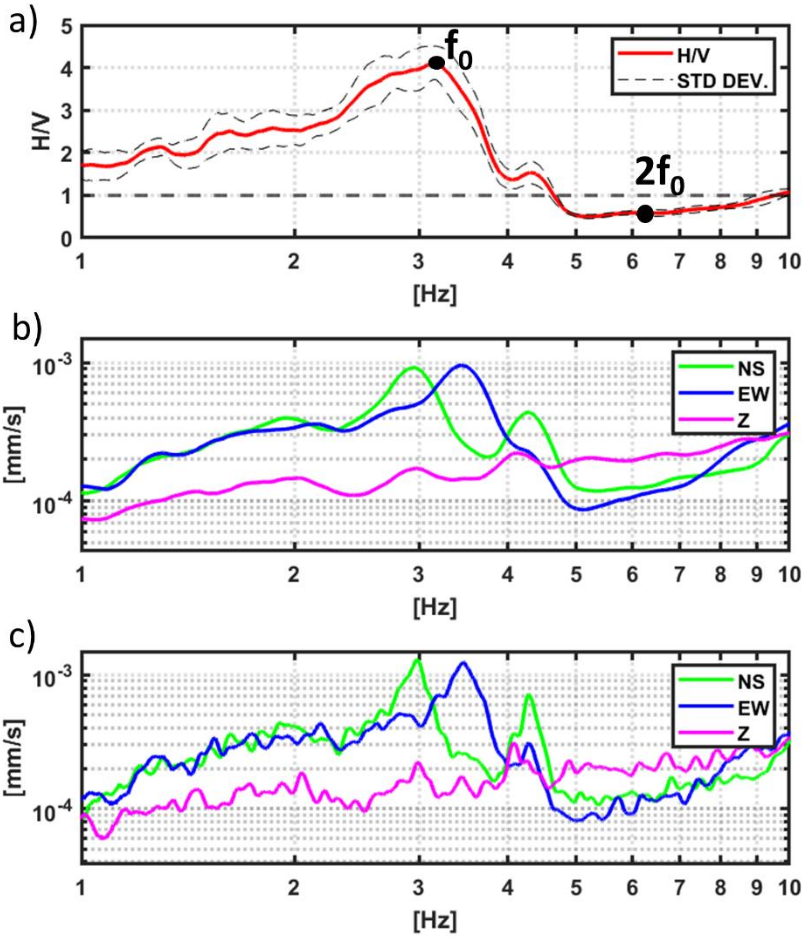

Figure 3. Non-stratigraphic H/V peaks induced by a viaduct with 30 m heigh pillars at approximately 80 m distance: a) H/V curve and b) corresponding amplitude spectra of the three components of motion with a 10% (of the central frequency) smoothing. c) is as b) but non-smoothed. The narrow spikes, occurring at different frequencies and with different amplitudes along different directions, have a clear non-stratigraphic origin.

In Table 1 we summarize the main features distinguishing stratigraphic from non-stratigraphic H/V peaks.

Table 1. Main differences between stratigraphic and non-stratigraphic H/V peaks.

STRATRIGRAPHIC H/V PEAKS (1D CONDITION)	**STRATRIGRAPHIC H/V PEAKS (non-1D CONDITION)**	**NON- STRATIGRAPHIC H/V PEAKS**
- Statistically coincident horizontal spectral components - H/V peak at frequency f_0, H/V trough at approx. $2f_0$ - the horizontal components can be flat at f_0 or show a local maximum - local minimum in the vertical component at f_0, local maximum at approx. $2f_0$ - H/V peaks are thus broad - H/V ~ 1 beyond the peak frequency range	- Horizontal components show peaks at different frequencies - As a consequence, the H/V peaks appear even broader than in the 1D case	- Narrow peaks with different spectral amplitudes and/or frequencies on different spectral components - better detectable in non-smoothed spectra or by using azimuthal processing - the corresponding H/V peaks (or troughs) appear much narrower than in the stratigraphic cases

In some other cases the spectral pattern behind H/V peaks is not fully clear: sometimes due to installation instabilities of the sensor. An example is given in Figure 4, where the H/V peak passes the SESAME criteria, the average NS component is larger than the others in the whole frequency domain and the other spectral components show patterns that cannot be fully reconducted to the cases described in Table 1. We will classify these cases as “other”.

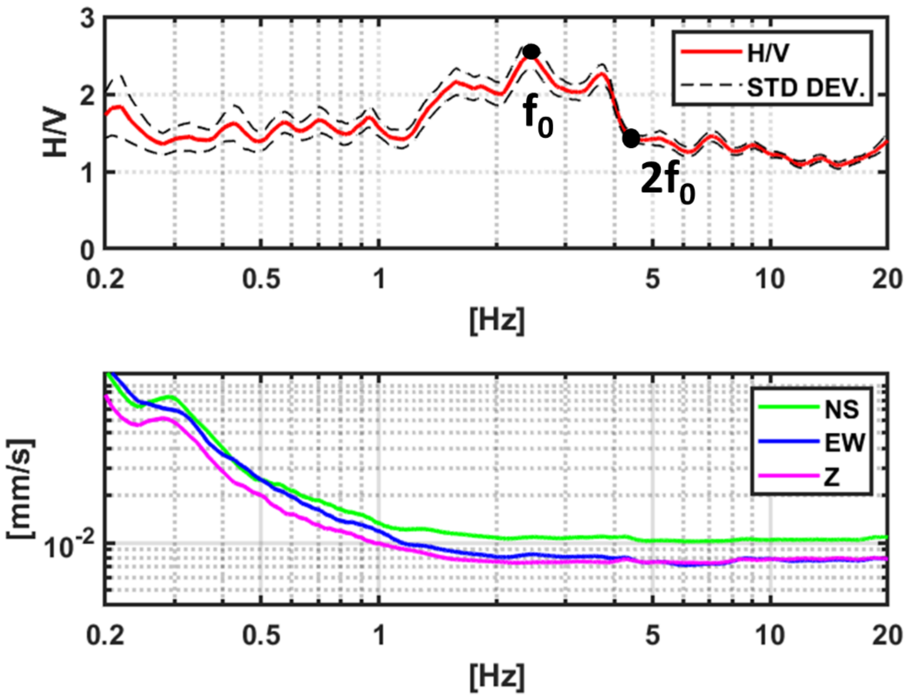

Figure 4. H/V peaks of unclear origin. The NS spectral component is amplified compared to the EW component in a wide frequency interval and no clear spectral pattern as those summarized in Table 1 can be acknowledged. The H/V curve was obtained by averaging the H/V obtained from several 30 s windows; the NS_{avg}, EW_{avg}, Z_{avg} spectra were obtained by averaging the spectra from the same 30 s windows. The H/V curve in the upper panel is therefore not the result of the division of the $\frac{\sqrt{NS_{avg} * EW_{avg}}}{Z_{avg}}$ spectra shown below.

ANN and CNN approaches

Distinguishing stratigraphic from non-stratigraphic H/V peaks for a human eye is often, though not always, a feasible task, following the indication listed in Table 1. This makes it possible for a human expert to prepare a dataset of stratigraphic, non-stratigraphic and ambiguous cases and provide such dataset to a supervised neural net for training.

To this aim, we trained both an Artificial Neural Network (ANN) and a Convolutional Neural Network (CNN).

ANN are inspired by the structure of the human brain and consist of interconnected layers of ‘neurons’ (nodes). Each node of a layer is connected to all the nodes of the successive layer and these connections are represented by a weight and biases (Bishop, 2006). In order to achieve the capability to perform automatic classification, a supervised neural network must be trained. During the training phase, a number of examples are presented to the net, together with the desired output and the weights associated to each link change to achieve the desired output. Once the network has been trained, the weights do not change anymore, and new input can be presented to the net to be classified accordingly.

The CNN architecture, originally inspired by the functioning of the animal visual cortex (Hubel & Wiesel, 1968; Fukushima, 1980; Yann, 1990), proved to be suitable to image classification tasks. Typically, a CNN consists of three main types of layers: convolutional, pooling, and fully connected layers. The convolutional and pooling layers are responsible for extracting relevant features from the input image, while the fully connected layer maps these features to the final output, that provides the classification.

A crucial step in the training of both these networks is thus the selection of the significant parameters to be extracted to form the training dataset. These are described in the following paragraphs.

ANN and CNN dataset preparation

The extraction of the parameters from the training database that will constitute the input for the neural network has to be based on the features that make the H/V peak classification possible. From Table 1 and Figure 1, Figure 2, Figure 3 it is clear that the individual spectral components are more informative about the nature of the H/V peaks, compared to the H/V curves themselves. For this reason, we will use as input the individual spectra and not their ratio. H/V is used in practice to compensate for the amplitude variations of the individual spectra (i.e., to compensate for the source effect) but here we will use a different form of compensation, not to lose information about significant differences between the horizontal components.

Our training database consists of 261 H/V peaks – passing the SESAME criteria – extracted from 184 microtremor recordings, all of duration larger than 20 min, collected at several different sites in Italy and classified by us as stratigraphic, artefactual or unknown/other. The H/V peak frequency distribution for the selected examples is illustrated in Figure S1 in the electronic supplement. This provides some information about the bedrock-like layer depth at the selected sites. We see that the most part of the selected examples was characterized by bedrocks at mid-to-large- depths (frequencies below 6 Hz).

Each of the 184 recordings available was divided into 70 s non-overlapping windows, detrended, tapered, fast Fourier–transformed, and smoothed with a triangular window with width equal to 10% of the central frequency. We tested different smoothing functions (triangular and cosinusoidal with variable width from 1 to 10% the central frequency) because non-stratigraphic peaks are more easily identifiable on poorly smoothed spectra (Figure 2 and Figure 3). However, we observed that the performance of the neural nets was not significantly affected by the smoothing percentage. Therefore, we used 10% smoothing as a final choice. Outlier windows showing spectra beyond two standard deviations from the mean were removed from the analysis in order to analyze only average H/V curves with narrow standard deviation. This is an important processing step, as we discuss in the Appendix.

At the end of the processing, we thus had 3 spectra (NS, EW, Z) and a H/V curve, where the H/V ratio is given by the geometric mean of the horizontal components divided by the vertical one $\frac{\sqrt{NS * EW}}{Z}$.

From each H/V curve that we wanted to classify, we extracted the main peaks according to their prominence. Form each peak, a virtual horizontal line was traced to the left and right, until it crossed the H/V curve because of the presence of another peak (or because the H/V curve ended). The minimum of the signal was searched in the two frequency intervals just defined to the right and to the left of the H/V peak. This point will either be a trough or the curve endpoint. The larger of the two interval minima becomes the reference level and the height above this level is here called ‘prominence’ (Figure S2 in the electronic supplement). We classified the H/V peaks according to their prominence and selected for classification up to a maximum of 3 peaks for each H/V curve.

Once the prominent peaks have been identified, occurring at frequency f_0, a window centred at f_0 and with a total aperture of $\Delta f = \left[\frac{f_0}{2}, 2f_0\right]$ is considered. Within this window, we resampled each individual spectrum with 30 points and this set of 30 values for each NS, EW, Z component (90 values) was the input provided to the neural net. We tested different number of samples (from 15 to 90) per training example and found that 30 was the smallest number capable to not reduce the neural network performance significantly. The aperture $\Delta f = \left[\frac{f_0}{2}, 2f_0\right]$ for each training example appeared sufficient to include the $[f_0, 2f_0]$ interval, diagnostic of the nature of the H/V peaks (Table 2a, Figure 5, Figure 6).

Since a huge variability in terms of spectral amplitude can exist in this $\Delta f = \left[\frac{f_0}{2}, 2f_0\right]$ range, depending on the local ambient noise level, on whether the data are in counts of physical units, etc., in order to simplify the artificial neural net training, we scaled the spectra by dividing each of them by the minimum value of the vertical component.

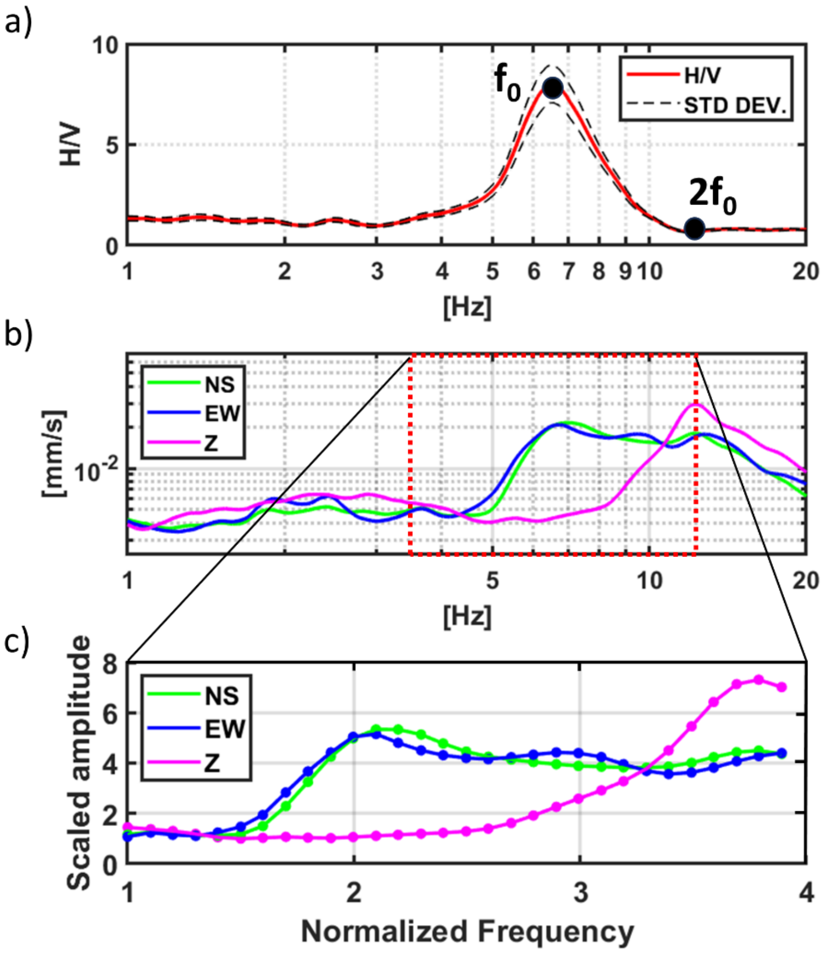

Figure 5. a) H/V curve and b) individual amplitude spectra (in velocity). The red frame centered around the H/V peak at f_0 = 6.5 Hz has a width $\Delta f = \left[\frac{f_0}{2}, 2f_0\right]$ and spans the [3.25, 13] Hz frequency interval. The spectra in this window range from amplitude 4 mm/s to 20 mm/s. The spectra within the red frame, scaled dividing them by their minimum vertical value, and resampled with 30 samples per component (panel c) constitute one input example for the ANN. Scaling the amplitude is important to compensate for the variability of the source and make the ANN work simpler. Frequencies are also normalized (1 stands for $\frac{f_0}{2}$; 2 stands for f_0; 4 stands for $2f_0$). The spectral shape is thus preserved, and the input values remain restricted into homogeneous intervals.

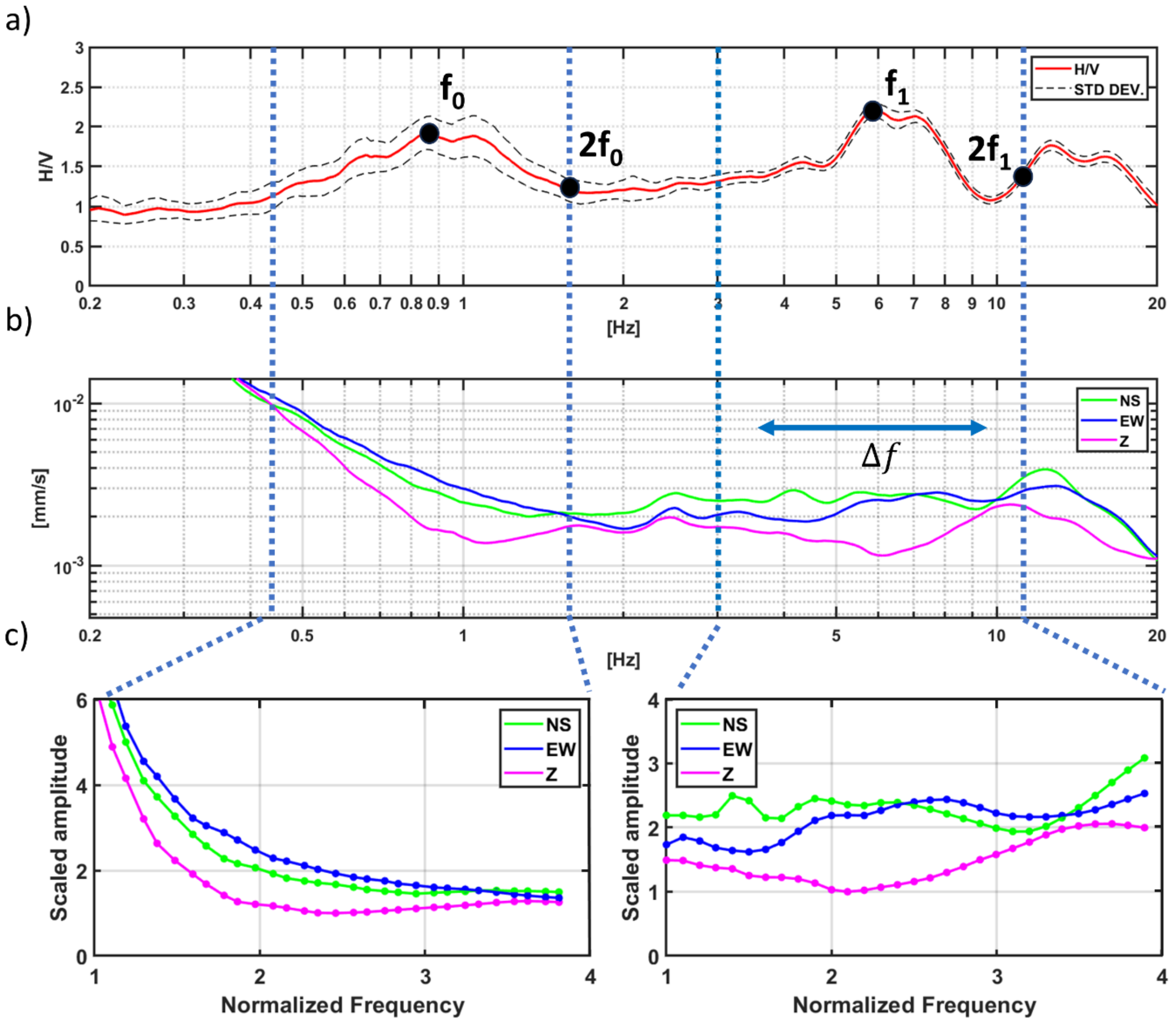

Figure 6. a) In this example two prominent peaks are identified at f_0 = 0.9 and f_1 = 6 Hz in the H/V curve. b, c) The corresponding spectra to be used as input for the ANN and CNN are thus extracted in the Δf_0 = [0.45, 1.8] Hz and Δf_1 = [3, 12] Hz intervals. The normalization and resampling procedures are the same described for Figure 5.

ANN architecture

Once the input examples and data have been defined, the ANN can be trained, which consists in adjusting the weights of the neuron connections to achieve the maximum output value at the expected class (stratigraphic, artefactual, other).

The input dataset was thus split into a training (70%) and a validation (30%) set.

The performance of the ANN in terms of mean square error (MSE) between predicted and expected output was then evaluated. Before reaching the final configuration, we tested different network architectures (i.e., different number of hidden layers (from 1 to 7) and of neurons (from 5 to 90), different activation functions (sigmoid, linear), different training algorithms (scaled conjugate gradient backpropagation, conjugate gradient backpropagation with Polak-Ribiére updates) and different training/validation subsets. We obtained the best performance (MSE = 0.0032) with an architecture of 7 hidden layers, each with [5, 10, 10, 10, 10, 10, 5] neurons respectively, activated by a hyperbolic tangent activation function and softmax (Bishop, 2006) activation function applied to the output layer only.

The best performing training algorithm for this type of classification was the Levenberg-Marquardt backpropagation (Marquardt, 1963; Hagan & Menhaj, 1994).

The performance of the finally selected classification model is shown in the confusion matrix of Table 2a. The precision rate is calculated as the ratio between the number of correct predictions to the total number of predictions. The recall rate measures the sensitivity of the model, and it is the ratio of correct predictions for a specific target to the total number of cases in which it occurs. The overall accuracy represents the total number of correct predictions among all the examples presented for the classification and was about 92% in the validation dataset. The elements outside the diagonal represent the misclassifications.

CNN

The input of convolutional neural nets are typically images. This does not require extracting points from the spectra but requires some scaling in the input images, so that they are all presented in the same way and the CNN goals can be easier to achieve.

We used a pretrained supervised SqueezeNet model (Iandola et al., 2016) and the same set of 261 H/V peaks used for the ANN, for the training phase. The SqueezeNet we used was trained on more than one million images from the ImageNet database (Russakovsky et al., 2015) and is made available by Matlab (Mathworks Inc., 2022). The entire network is composed of 68 layers and 75 connections. The requested image input size is 227 x 227 pixels and can be a RGB image. We note that such a matrix of values is much larger than the 90 input values used in the ANN and we could reasonably achieve the same results with smaller matrices. However, processing H/V images is certainly an option (for example when one does not have the data but only the H/V + spectra figure) and we believed that exploring the performance of a network pre-trained on image pattern recognition was interesting, too.

In a pre-trained network like SqueezeNet, when a new convolutional layer is added at the end of the network, the previously learned feature maps is still used. These feature maps were learned during the pre-training process on a large dataset and were already optimized for identifying general patterns in the input data. By utilizing the learned feature maps, a neural network can quickly adapt to a new task by fine-tuning the weights of a newly added layer on a smaller, task-specific dataset. This process is known as transfer learning (Pratt, 1993) and has shown to be effective, particularly when the new dataset is relatively small.

However, when fine-tuning the network, it is necessary to adjust a range of parameters that control the model, as well as hyperparameters that control the training process, to let the network learn the relevant features of the new dataset.

It was thus necessary to modify the last layers (last convolution 2D Layer and classification output layer) without resetting the weights obtained for the first layers and retrain the network on our database. The feature of this neural network is that, unlike some other NNs, its final layer is a convolutional layer instead of a fully connected layer. In fully connected layers, each neuron is connected to all neurons in the previous layer. This is typical in ANN. Differently, in this CNN, the final layer is another convolutional layer, where neurons perform convolution operations on the input data. This allows to preserve the spatial information of the image and perform a more precise classification. The function used to train the network is a stochastic gradient descent with momentum and the loss function is the cross-entropy loss.

The hyperparameters of the neural network were tuned as follows: the initial learning rate was set to 0.0001, which controls the rate of weight updates during the gradient descent algorithm used to minimize the network loss function. The maximum number of epochs was set to 8, which limits the duration of the training process and prevents overfitting. The batch size was set to 11, which is the number of training examples used in each iteration of the training process. Each epoch involved iterating through all the batches of the dataset to update the weights of the network. This allowed the network to learn from the entire dataset without requiring all the data to be loaded into memory at once.

As per the ANN, the dataset was divided into a training and a validation subset, with 70% and 30% examples respectively, extracted from the prepared database.

We obtained an overall accuracy (percentage of examples classified correctly out of the total number of examples) on the validation set of about 95%, as shown in Table 2b.

The final ANN and CNN architectures are summarized in Figure 7.

Table 2. a) Performance of the trained ANN. Precision is the number of correct predictions to the total number of predictions. Recall rate is the number of correct predictions for a specific target to the total number of cases where the target occurs. The overall accuracy is the total number of correct predictions among all the examples presented for the classification. b) Performance of the trained CNN. Precision is the number of correct predictions to the total number of predictions. Recall rate is the number of correct predictions for a specific target to the total number of cases where the target occurs. The overall accuracy is the total number of correct predictions among all the presented examples to classify.

a)	Real target			
Predicted target	Stratigraphic	Artefactual	Other	Precision
Stratigraphic	27	1	0	96.4%
Artefactual	1	24	3	85.7%
Other	1	0	21	95.4%
Recall	93.1%	96.0%	87.5%	
Overall Accuracy				92.3%

b)	Real target			
Prediction target	Stratigraphic	Artefactual	Other	Precision
Stratigraphic	29	2	1	90.6%
Artefactual	0	22	1	95.6%
Other	0	0	23	100.0%
Recall	100%	91.7%	92.0 %	
Overall Accuracy				94.8%

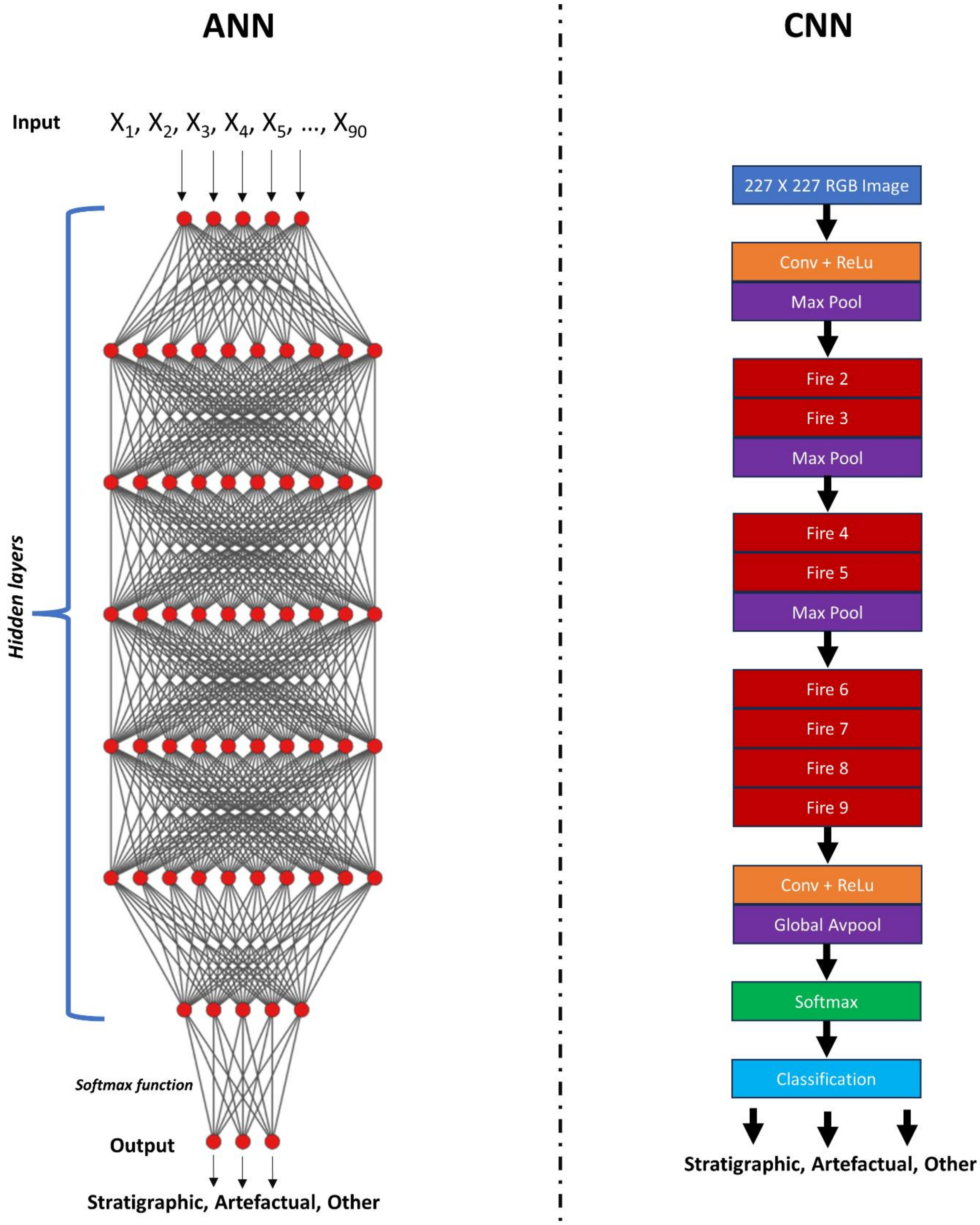

Figure 7. Schematic architecture of the Artificial Neural Network (left) and of the Convolutional Neural Network (right) used in this study. The input of the ANN is a matrix of 30 (scaled spectral amplitude, normalized frequency) values per component (90 values per example); the input of the CNN is a 227 x 227 RGB pixel image of the same normalized spectra. In detail, 'Conv' represents a convolutional layer with a corresponding ReLU (activation function). 'Fire' is a convolutional block with 1x1 and 3x3 convolutions designed to extract information. 'Max Pooling' is employed for dimension reduction by selecting the maximum value in a window. 'Global Average Pooling' is utilized for dimension reduction by calculating the average of the output. Lastly, 'Softmax' assigns probabilities to classes (for more detail see Iandola et al., 2016).

Comparison of the ANN and CNN performances on a fully independent dataset

We tested the trained ANN and CNN on an independent dataset from the ARRA-funded (American Recovery and Reinvestment Act, 2009) site characterization project. Within this project, 184 Californian strong-motion stations sites were characterized by means of geophysical surveys (including microtremor H/V), as well as 4 stations in the Central-Eastern United Sates (CEUS) (Yong et al., 2013). All data were collected for one hour at 200 samples per second and three to six recordings were collected at each investigated site.

All these data were reprocessed and resampled by us, in the same way used to prepare the training set.

From a total amount of about 600, we retained 168 ambient noise recordings and a total amount of 220 peaks to be classified. Those excluded did not contain peaks (seismic stations are often installed on outcropping rock) or had a too large standard deviation, which made them statistically unreliable.

Each prominent peak was both classified by a human operator (us) and classified from the ANN and CNN into the three available classes. The human operator classified the possible output with a binary code [0,0,1] for 'stratigraphic'; [0,1,0] for 'artefactual' and [1,0,0] for 'other' peak. The NN output is a number in the range [0 1] that indicates the probability assigned to each class. From Table 3a we see that the test dataset contains, according to the human operator, 89% stratigraphic, 5.5% artefactual and 5.5% other peaks.

We now discuss the performance of our nets in the classification of stratigraphic and non-stratigraphic (anthropic, other) peaks from this dataset.

From the preliminary confusion matrix, we see that peaks classified as stratigraphic by humans, are also classified as such from CNN and ANN in 92.3% and 80.6% of cases, respectively.

The overall accuracy (percentage of examples classified correctly out of the total number of examples) on this fully independent dataset is 91.4% and 79.5% for ANN and CNN, respectively.

We note that a different classification between the nets and human output does not necessarily imply an error on either side. When the network suggests a different class compared to human experience, a closer examination of the corresponding H/V curve and spectra should be performed, as they may reveal patterns not immediately understood by the human eye or *vice-versa*.

To present a more visual comparison, in Figure 8a, we show the probability of attribution to the stratigraphic class for each input example, where the blue bars indicate when the network attribution coincides with the human classification, and the orange bars indicate when it diverges. The height of each bar represents the confidence of the attribution of the specific example to the corresponding class in the range [0, 1] given by the neural nets.

For the 'stratigraphic class', CNN provides a different classification compared to human classification in 15 cases out of 196, while ANN in 38 cases. Figure 8b and Figure 8c shows the same results for the non-stratigraphic and other class, respectively. The CNN achieved 100% precision (12 correctly classified cases out of 12) for the 'artefactual class', while the ANN gave 5 apparently incorrect cases out of 12. On the other hand, for the 'other class', the CNN achieved a precision of 66% with 4 out of 12 cases apparently misclassified, while the ANN achieved 83% precision with only 2 apparently misclassified cases.

At this point it is important and interesting to study the reasons for these classification differences. We will thus analyse the cases where either one or both networks disagree with human classification.

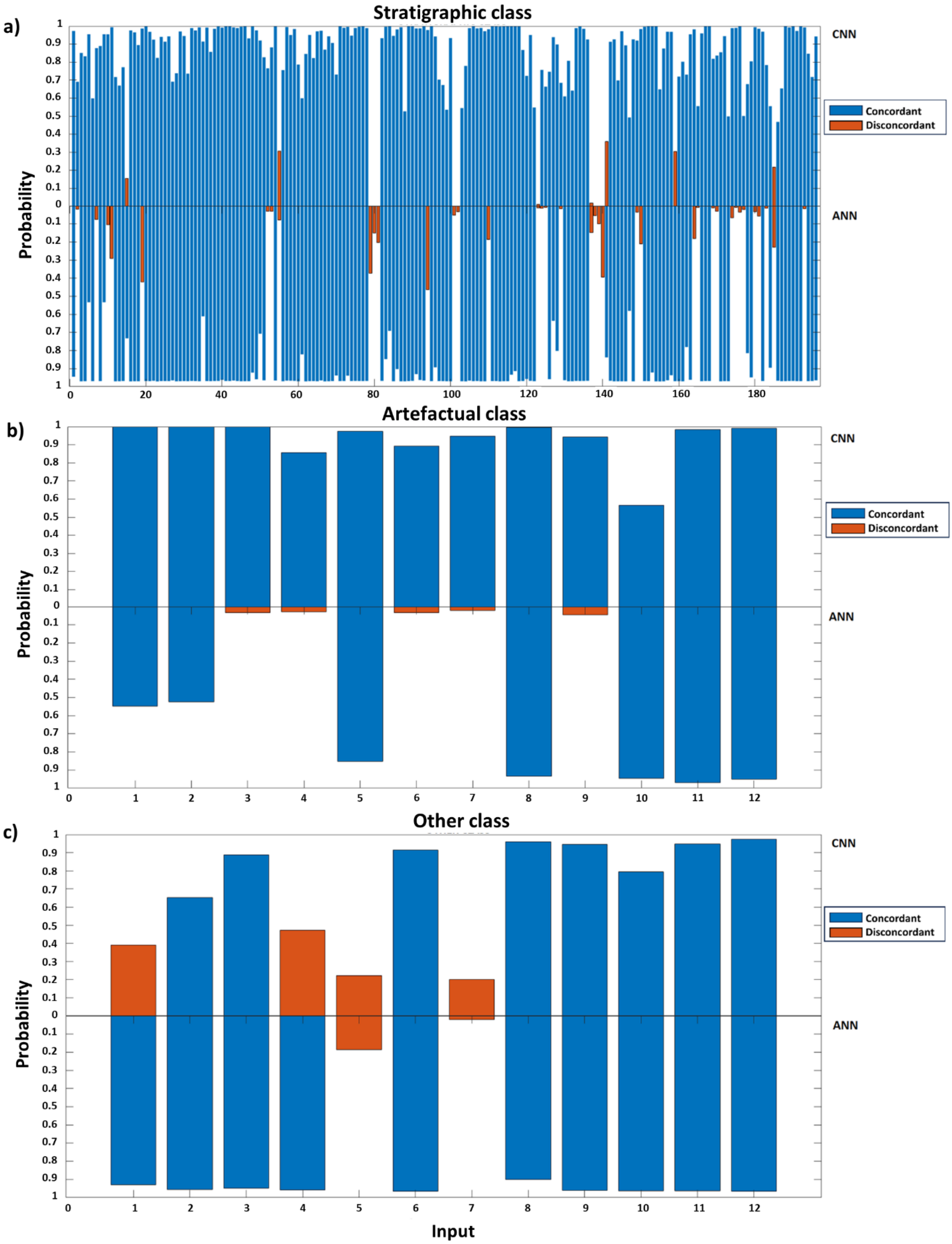

Figure 8. a) Confidence of attribution of each example to the stratigraphic class according to the CNN (top half) and ANN (bottom half) networks. For these examples the expected output is the 'stratigraphic' class. Blue bars mark the examples for which also the neural nets provided a classification as stratigraphic. Orange bars mark the examples classified into a different class by the nets. b) Confidence of attribution of each example to the artefactual class according to the CNN (top half) and ANN (bottom half) networks. For these examples the expected output is the 'artefactual' class. Blue bars mark the example for which also the neural nets provided a classification as artefactual. Orange bars mark the examples classified into a different class by the nets. c) Confidence of attribution of each example to the other class according to the CNN (top half) and ANN (bottom half) networks. For these examples the expected

output is the 'other' class. Blue bars mark the example for with also the neural nets provided a classification as 'other'. Orange bars mark the examples classified into a different class by the nets.

Discussion

The cases in which the networks disagree with human classification can be categorized, with reference to the stratigraphic class, into two types: i) presence of stratigraphic H/V peaks with superimposed artefacts; ii) multiple H/V peaks at close distance.

As an example of the first case, let us consider Figure 9. This example shows a clear stratigraphic H/V peak at 1.5 Hz, disturbed by a number of artefacts, the most prominent of which occur at 1.4 and 1.8 Hz (panel a, b). When these are removed by filtering the recording, the stratigraphic nature of the H/V peak is even more evident (panel c, d).

This example was classified as stratigraphic by the human operators because in training the net it was not possible to provide two possible outputs for the same input. However, CNN and ANN respectively assign a probability of 30% and 4% to the stratigraphic class; of 70% and 93% to the artefactual class, correctly acknowledging the simultaneous presence of artefacts. These cases cannot therefore be considered as misclassified. This pattern occurred 3 times in our dataset and the the preliminary confusion matrix (Table 3a) changes to what is shown in Table 3b. The network rate of success increases to 92.7% and 80.9%, respectively.

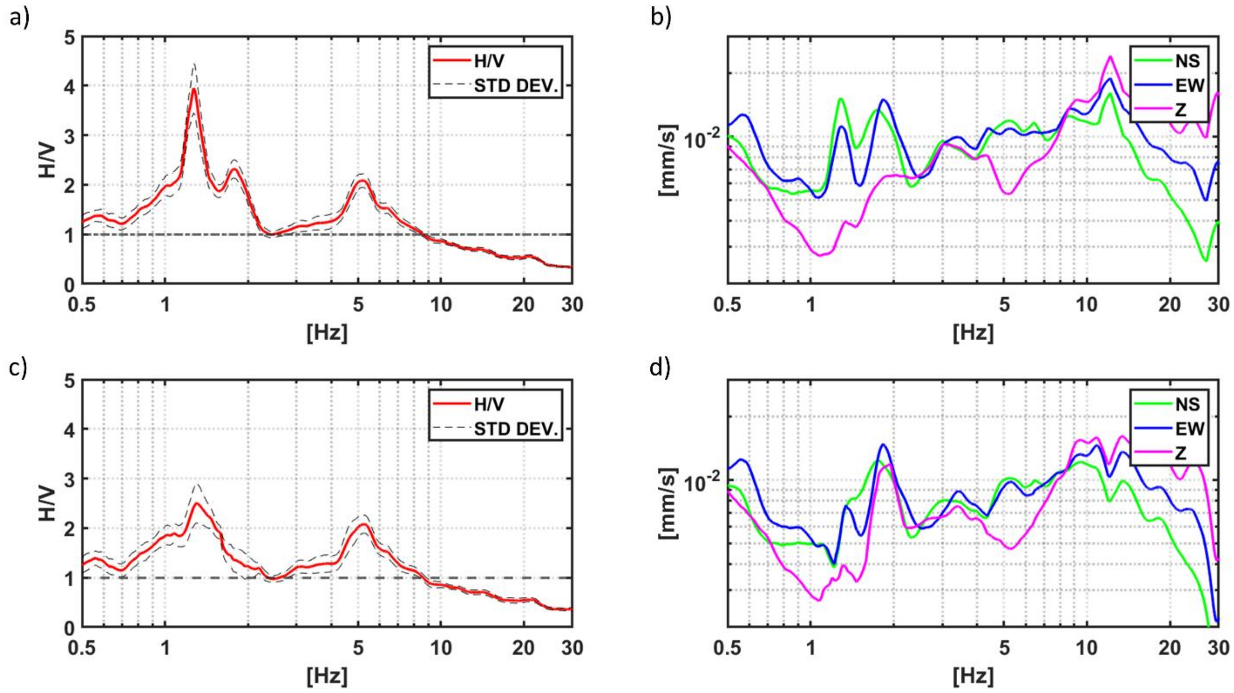

Figure 9. Example of H/V curve with stratigraphic peaks at 1.5 and 5 Hz, with superimposed artefacts: (a, b) original H/V curve and corresponding amplitude spectra of the three components of motion; (c, d) H/V curve and corresponding spectra after a notch-filter

application to reduce the main artefactual disturbances. The stratigraphic origin of the 1.5 and 5 Hz peaks is clearly suggested by the local minima in the vertical spectral component of motion.

Table 3. a) Preliminary confusion matrix for CNN (left) and ANN (right). The sample test contained 220 examples (196 classified by human operators as stratigraphic, 12 as artefactual and 12 as other). b) Final confusion matrix for CNN (left) and ANN (right). The sample test contained 220 examples (196 classified by human operators as stratigraphic, 12 as artefactual and 12 as other).

a)	CNN			ANN		
	Actual target			Actual target		
Predicted target	Other	Artefactual	Stratigraphic	Other	Artefactual	Stratigraphic
Other	8	0	4	10	5	21
Artefactual	1	12	11	2	7	17
Stratigraphic	3	0	181	0	0	158
Recall	66.7%	100.0%	92.3%	83.3%	58.3%	80.6%
Overall Accuracy			91.4%			79.5%

b)	CNN			ANN		
	Actual target			Actual target		
Predicted target	Other	Artefactual	Stratigraphic	Other	Artefactual	Stratigraphic
Other	8	0	4	10	5	21
Artefactual	1	12	8	2	7	14
Stratigraphic	3	0	184	0	0	161
Recall	66.7%	100.0%	93.8%	83.3%	58.3%	82.1%
Overall Accuracy			92.7%			80.9%

The second group of misclassifications arises when in the $\Delta f = \left[\frac{f_0}{2}, 2\mathrm{f}_0\right] f_0$ window selected around the prominent H/V peak, a second H/V peak (or part of it) is present. In other words, when two H/V peaks occur in a narrow frequency interval. An example is provided in Figure 10 (a,b), where the $\Delta f = \left[\frac{f_0}{2}, 2\mathrm{f}_0\right]$ window around the prominent peak includes part of another apparent peak on the left side. In this case, both networks classify (with 99% and 96% confidence, respectively) the 3 Hz peak as an artifact. This pattern occurred 5 time in our dataset.

So far, we have discussed the divergence between the NNs and human classification, however, there are also cases where the CNN and ANN classifications diverge on the same examples. CNN seems to have more problems in identifying as stratigraphic peaks spectra those with weak local maxima in the horizontal components and less pronounced local minima in the vertical component compared to ANN. In these cases the CNN finds it hard to produce a unique answer and assigns large probabilities to all classes (e.g., 46% artefactual, 36% stratigraphic, 18% other for the 4.8 Hz peak in Figure 10 c,d).

In general, by also observing Figure 8a and Figure 8b, ANN seems to be less precise in this task compared to the CNN. This discrepancy can be attributed, beyond the specific differences between the two types of nets and input size, also to criteria that we had to apply to extract the input parameters from the spectra to train the ANN and that we did not have to make explicit for CNN.

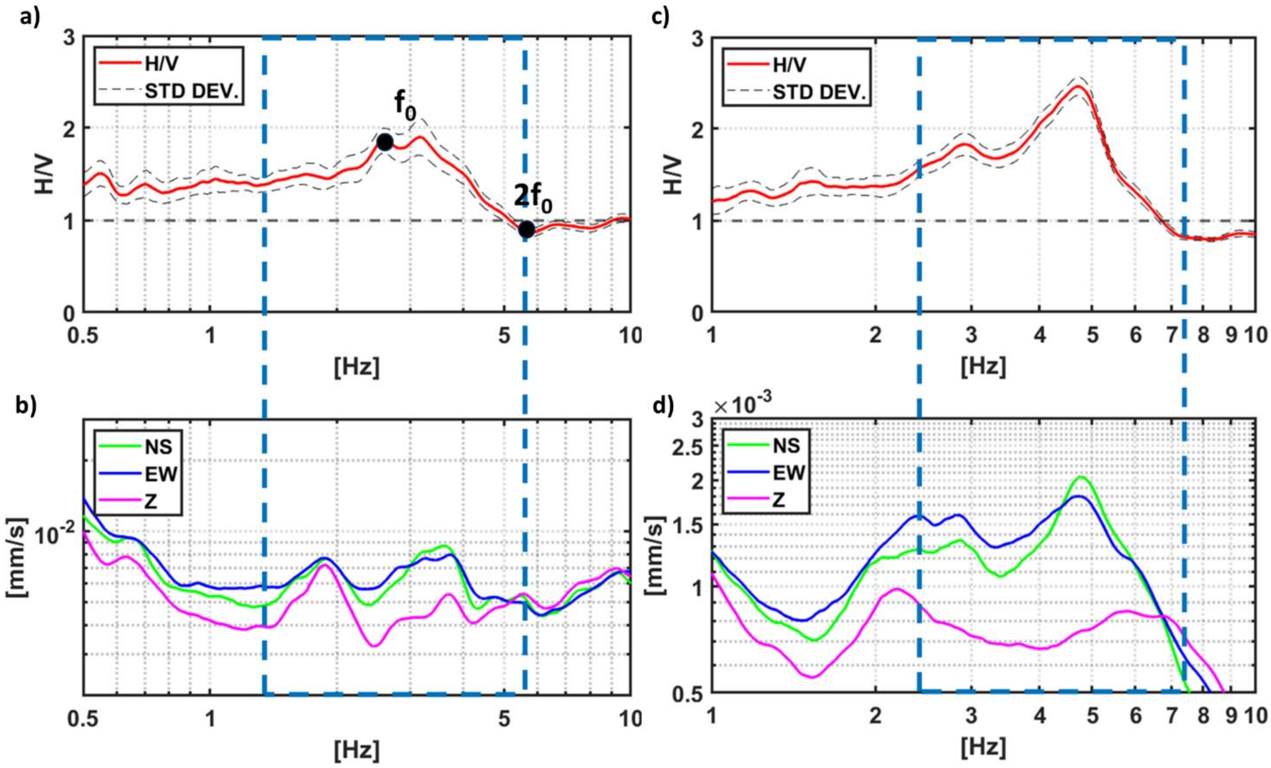

Figure 10. a) H/V curve of stratigraphic peak at 3.1 Hz and b) corresponding individual spectra of motion in velocity. The dashed blue lines indicate $\Delta f = \left[\frac{f_0}{2}, 2f_0\right]$ window used to identify the prominent peak and it is evident that the window includes, on the left side, part of another peak. c) H/V curve with a stratigraphic peak at 4.8 Hz and d) corresponding individual spectra of motion in velocity. The dashed blue frame indicates the $\Delta f = \left[\frac{f_0}{2}, 2f_0\right]$ window used to identify the prominent peak. This example was classified by CNN as 46% artefactual, 36% stratigraphic, 18% other and this is understandable for several reasons: the horizontal components are not statistically identical and there is more than one local maxima in each horizontal component within the selected frequency interval.

Conclusions

Seismic networks, seismic microzonation surveys and seismic exploration of the subsoil provide thousands and thousands of microtremor recordings all around the globe. When processed in terms of H/V spectral ratios, these can unveil useful stratigraphic features about the subsoil. However, it is mandatory to distinguish stratigraphic from non-stratigraphic features before any interpretation. In this paper we first review what makes a H/V peak stratigraphic or not. Then, we train two types of supervised neural nets to classify H/V peaks automatically, or at least to support human decisions by means of an extended knowledge base.

We trained an ANN that uses as input a set of sorted values extracted from the individual microtremor spectra. Then, we trained a CNN working directly on images of the microtremor spectra. In both cases the data were scaled to span a common range of size and values, to make the nets work easier. The nets were trained on an Italian dataset of H/V curves and tested on an independent dataset of Californian curves, collected by different instruments but processed in the same way. On a fully independent database compared to the training one, the two nets respectively showed 81 and 93% accuracy in classifying the presented input, compared to the human choices.

In this specific task, using a CNN is more convenient than ANN. The former does not require the extraction of specific input values from the individual spectra (and all the problems connected to the choice of the most suitable number of input data, for example) but allows to achieve a classification directly from an image. It must be noted, however, that this is the case because we used a pre-trained CNN where the optimization of the parameter extraction from the images was already implemented. However, the CNN still seems to have a slightly larger generalization capability in this case.

Some of the independent examples presented to the networks did not fall in single output class but showed both artefacts and stratigraphic peaks in the same example. Our training dataset did not include such phenomenology, but the nets still managed to classify them as belonging with equal probability to two classes.

These results were obtained on relatively small training databases, composed of approximately 200 examples and with a large unbalance in number of examples for the three output categories. Such an unbalance somehow reflects the real-world distribution but can be a limitation in the NN training.

Discriminating artefactual from stratigraphic peaks in microtremor recordings is compulsory before any use of the data but this is a quite neglected step. It is quite impressive that the H/V curves are still very rarely analysed together with the individual components of motion, which is where the origin of the peaks can better be assessed. The proposed approach can support the operators and the automatic processing systems in their decisions, as well as complement the SESAME criteria.

Data and Resources

The data used to train the networks come from SC's personal archive. The data used to test the networks come are publicly accessible and come from https://pubs.usgs.gov/of/2013/1102/ (last accessed August 2022). The electronic supplement includes two figures quoted in the text (Figure S1-S2) and information about the H/V curves used to train the neural nets.

Declaration of competing interests

The authors acknowledge there are no conflicts of interest recorded.

Acknowledgments

The authors warmly thank the two anonymous reviewers and the associate editor for their careful revision and valuable suggestions.

Appendix

The SESAME (2004) guidelines recommend ensuring the statistical significance of the H/V peaks before interpreting them. The H/V curves are generated by splitting the recorded signals into windows and by computing the spectral ratio on each. The final H/V curve is their average. Sometimes, isolated disturbed windows (typically those where the operators stand too close to the seismometer) significantly alter the spectral ratios. Let us consider the average H/V curve and the corresponding spectra obtained by splitting a microtremor recording into 70 s windows (Figure A1). The spectrogram (Figure A1e) clearly shows that a few of these windows significantly differ from the others. Once these transients have been removed (see Castellaro and Mulargia, 2009 for the procedure followed to remove them), the standard deviation around the individual spectra and the H/V ratio becomes acceptable and the spectral pattern turns back to its typical feature (eye-shape around f_0) described in Figure 1.

If we present to the networks the uncleaned data (Figure A1a, c) these would be wrongly classified as stratigraphic while presenting to the networks the cleaned data (Figure A1b, d) turns into a correct classification.

If we look at the positive side, misclassifications from the neural nets could sometimes mark poorly cleaned recordings (i.e. recordings where transients were not sufficiently removed).

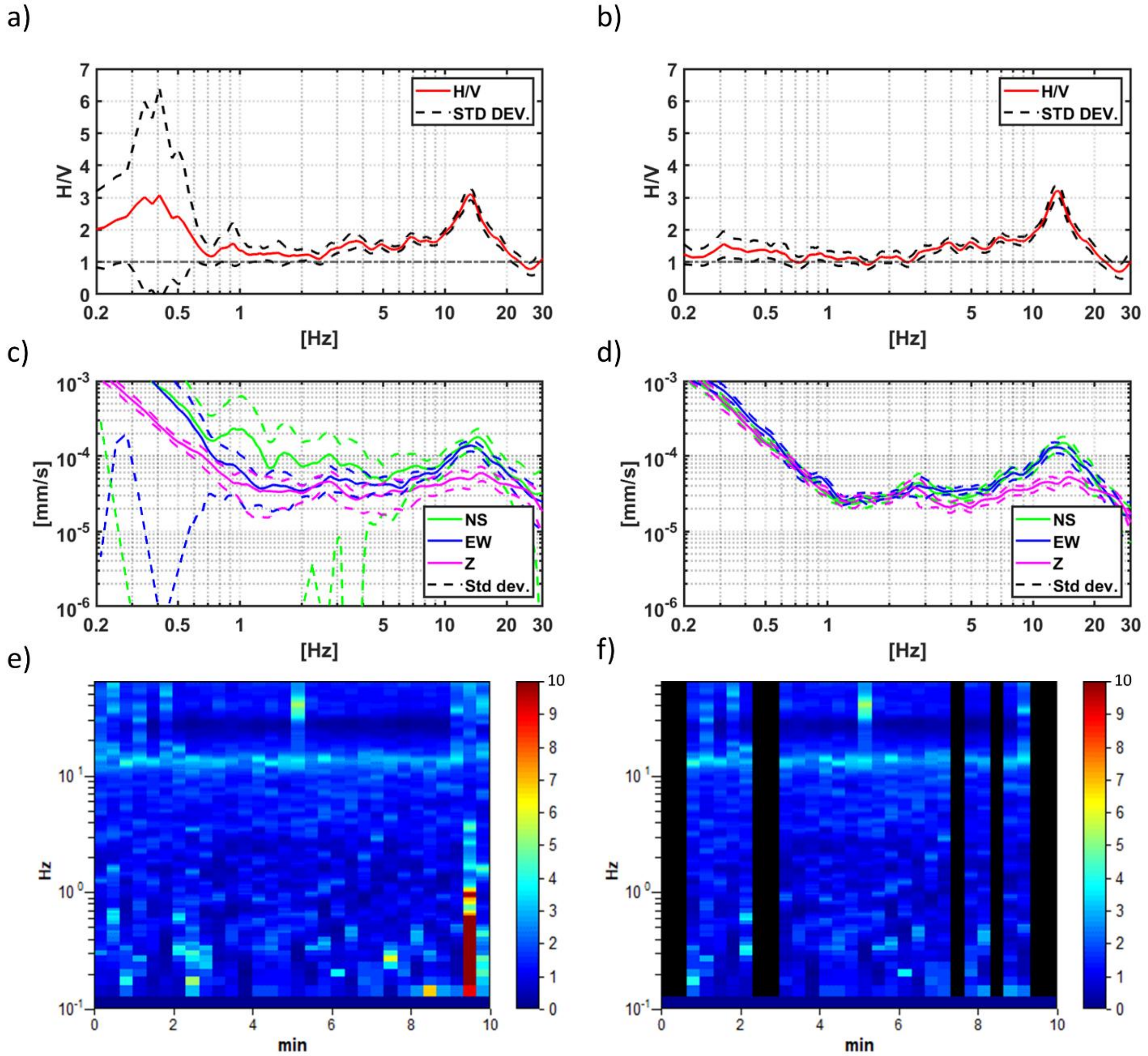

Figure A1. Average H/V curves and their standard deviations recorded at the same site before (a) and after (b) transient removal. Corresponding individual spectra of motion in velocity and standard deviation for individual components before (c) and after (d) transient removal. e) Time stability of the H/V curve during the measurement (H/V amplitude in color, time on the x-axis, frequency on the y-axis) and d) remaining time windows after transient removal.

Bibliography

Bard, P.-Y., & Bouchon, M. (1980a). The seismic responce of sediment-filled valleys. Part 1. The case of incident SH waves. *Bulletin of the Seismological Society of America*, *70*(4), 1263–1286.

Bergamo, P., Hammer, C., & Fäh, D. (2021). On the Relation between Empirical Amplification and Proxies Measured at Swiss and Japanese Stations: Systematic Regression Analysis and Neural Network Prediction of Amplification. *Bulletin of the Seismological Society of America*, *111*(1), 101–120. https://doi.org/10.1785/0120200228

Bishop, C. M. (2006). *Pattern Recognition and Machine Learning*. Springer.

Bokelmann, G. H. R., & Baisch, S. (1999). Nature of narrow-band signals at 2.083 Hz. *Bulletin of the Seismological Society of America*, *89*(1), 156–164. https://doi.org/10.1785/BSSA0890010156

Bonnefoy-Claudet, S., Kohler, A., Cornou, C., Wathelet, M., & Bard, P.-Y. (2008). Effects of Love Waves on Microtremor H/V Ratio. *Bulletin of the Seismological Society of America*, *98*(1), 288–300. https://doi.org/10.1785/0120070063

Boudghene Stambouli, A., Zendagui, D., Bard, P.-Y., & Derras, B. (2017). Deriving amplification factors from simple site parameters using generalized regression neural networks: Implications for relevant site proxies. *Earth, Planets and Space*, *69*(1), 99. https://doi.org/10.1186/s40623-017-0686-3

Castellaro, S. (2016). The complementarity of H/V and dispersion curves. *GEOPHYSICS*, *81*(6), T323–T338. https://doi.org/10.1190/geo2015-0399.1

Castellaro, S., Alessandrini, G., & Musinu, G. (2022). Seismic Station Installations and Their Impact on the Recorded Signals and Derived Quantities. *Seismological Research Letters*, *93*(6), 3348–3362. https://doi.org/10.1785/0220220029

Castellaro, S., & Mulargia, F. (2010). How Far from a Building Does the Ground-Motion Free-Field Start? The Cases of Three Famous Towers and a Modern Building. *Bulletin of the Seismological Society of America*, *100*(5A), 2080–2094. https://doi.org/10.1785/0120090188

Castellaro, S., & Mulargia, F. (2009a). VS30 Estimates Using Constrained H/V Measurements. *Bulletin of the Seismological Society of America*, *99*(2A), 761–773. https://doi.org/10.1785/0120080179

Castellaro, S., & Mulargia, F. (2009b). The Effect of Velocity Inversions on H/V. *Pure and Applied Geophysics*, *166*(4), 567–592. https://doi.org/10.1007/s00024-009-0474-5

Castellaro, S., & Musinu, G. (2023). Resonance versus Shape of Sedimentary Basins. *Bulletin of the Seismological Society of America*, *113*(2), 745–761. https://doi.org/10.1785/0120210277

Cheng, T., Cox, B.R., Vantassel, J.P., Manuel, L., 2020. A statistical approach to account for azimuthal variability in single-station HVSR measurements. Geophys. J. Int. 223, 1040-1053. https://doi.org/10.1093/gji/ggaa342

Cornou, C., Guéguen, P., Bard, P.-Y., & Haghshenas, E. (2004). Ambient noise energy bursts observation and modeling: Trapping of harmonic structure-soil induced?waves in a topmost sedimentary layer. *Journal of Seismology*, *8*(4), 507–524. https://doi.org/10.1007/s10950-004-1980-7

Díaz, J. P., Sáez, E., Monsalve, M., Candia, G., Aron, F., & González, G. (2022). Machine learning techniques for estimating seismic site amplification in the Santiago basin, Chile. *Engineering Geology*, *306*, 106764. https://doi.org/10.1016/j.enggeo.2022.106764

Dreossi, I.,Barnaba C., Castellaro S. (2018). Book of Abstracts: 36th General Assembly of the European Seismological Commission, 2-7 September 2018, Valletta- Malta. (2018). Mistral Service.

Endrun, B. (2011). Love wave contribution to the ambient vibration H/V amplitude peak observed with array measurements. *Journal of Seismology*, *15*(3), 443–472. https://doi.org/10.1007/s10950-010-9191-x

Ermert, L., Poggi, V., Burjánek, J., & Fäh, D. (2014). Fundamental and higher two-dimensional resonance modes of an Alpine valley. *Geophysical Journal International*, *198*(2), 795–811. https://doi.org/10.1093/gji/ggu072

Fäh, D., Kind, F., & Giardini, D. (2001). A theoretical investigation of average *H/V* ratios. *Geophysical Journal International*, *145*(2), 535–549. https://doi.org/10.1046/j.0956-540x.2001.01406.x

Fukushima, K. (1980). Neocognitron: A self-organizing neural network model for a mechanism of pattern recognition unaffected by shift in position. *Biological Cybernetics*, *36*(4), 193–202. https://doi.org/10.1007/BF00344251

Ghasemi, H., Zare, M., Fukushima, Y., & Sinaeian, F. (2009). Applying empirical methods in site classification, using response spectral ratio (H/V): A case study on Iranian strong motion network (ISMN). *Soil Dynamics and Earthquake Engineering*, *29*(1), 121–132. https://doi.org/10.1016/j.soildyn.2008.01.007

Hagan, M. T., & Menhaj, M. (1994). Training feed-forward networks with the Marquardt algorithm. *IEEE Transactions on Neural Networks*, *5*(6), 989–993.

Hubel, D. H., & Wiesel, T. N. (1968). Receptive fields and functional architecture of monkey striate cortex. *The Journal of Physiology*, *195*(1), 215–243. https://doi.org/10.1113/jphysiol.1968.sp008455

Iandola, F. N., Han, S., Moskewicz, M. W., Ashraf, K., Dally, W. J., & Keutzer, K. (2016). *SQUEEZENET: ALEXNET-LEVEL ACCURACY WITH 50X FEWER PARAMETERS AND <0.5MB MODEL SIZE*. 14.

Ji, K., Ren, Y., Wen, R., Zhu, C., Liu, Y., & Zhou, B. (2022). HVSR-based Site Classification Approach Using General Regression Neural Network (GRNN): Case Study for China Strong Motion Stations. *Journal of Earthquake Engineering*, *26*(16), 8423–8445. https://doi.org/10.1080/13632469.2021.1991520

Konno, K., & Ohmachi, T. (1998). Ground-motion characteristics estimated from spectral ratio between horizontal and vertical components of microtremor. *Bulletin of the Seismological Society of America*, *88*(1), 228–241. https://doi.org/10.1785/BSSA0880010228

Lattanzi, G., Castellaro, S., & Di Donato, M. (2023). On the time-stability of resonance frequencies in deep basins. *Geophysical Journal International*, *234*(3), 1870–1884. https://doi.org/10.1093/gji/ggad172

Le Roux, O., Cornou, C., Jongmans, D., & Schwartz, S. (2012). 1-D and 2-D resonances in an Alpine valley identified from ambient noise measurements and 3-D modelling: *1-D and 2-D resonances in an Alpine valley*. *Geophysical Journal International*, *191*(2), 579–590. https://doi.org/10.1111/j.1365-246X.2012.05635.x

Marquardt, D. W. (1963). An Algorithm for Least-Squares Estimation of Nonlinear Parameters. *Journal on Applied Mathematics*, *11*, 431–441

Matsushima, S., Hirokawa, T., De Martin, F., Kawase, H., Sanchez-Sesma, F.J., 2014. The Effect of Lateral Heterogeneity on Horizontal-to-Vertical Spectral Ratio of Microtremors Inferred from Observation and Synthetics. Bull. Seismol. Soc. Am. 104, 381-393. https://doi.org/10.1785/0120120321

Molnar, S., Cassidy, J. F., Castellaro, S., Cornou, C., Crow, H., Hunter, J. A., Matsushima, S., Sánchez-Sesma, F. J., & Yong, A. (2018). Application of Microtremor Horizontal-to-Vertical Spectral Ratio (MHVSR) Analysis for Site Characterization: State of the Art. *Surveys in Geophysics*, *39*(4), 613–631. https://doi.org/10.1007/s10712-018-9464-4

Molnar, S., Sirohey, A., Assaf, J., Bard, P.-Y., Castellaro, S., Cornou, C., Cox, B., Guillier, B., Hassani, B., Kawase, H., Matsushima, S., Sánchez-Sesma, F. J., & Yong, A. (2022). A review of the microtremor horizontal-to-vertical spectral ratio (MHVSR) method. *Journal of Seismology*, *26*(4), 653–685. https://doi.org/10.1007/s10950-021-10062-9

Nakamura, Y. (1989). A method for dynamic characteristics estimation of subsurface using microtremor on the ground surface. *Quarterly Report of Railway Technical Research*, *3*(1), 25–33.

Oubaiche, E. H., Chatelain, J., Hellel, M., Wathelet, M., Machane, D., Bensalem, R., & Bouguern, A. (2016). The Relationship between Ambient Vibration H/V and SH Transfer Function: Some Experimental Results. *Seismological Research Letters*, *87*(5), 1112–1119. https://doi.org/10.1785/0220160113

Pratt, L. (1993). Discriminability-based transfer between neural networks. *NIPS Conference: Advances in Neural Information Processing Systems*, 204–211

Roten, D., Fäh, D., Cornou, C., & Giardini, D. (2006). Two-dimensional resonances in Alpine valleys identified from ambient vibration wavefields. *Geophysical Journal International*, *165*(3), 889–905. https://doi.org/10.1111/j.1365-246X.2006.02935.x

Rumelhart, D. E., & McClelland, J. L. (1986). *Parallel distributed processing: Explorations in the microstructure of cognition*. MIT Press.

Russakovsky, O., Deng, J., Su, H., Krause, J., Satheesh, S., Ma, S., Huang, Z., Karpathy, A., Khosla, A., Bernstein, M., Berg, A. C., & Fei-Fei, L. (2015). ImageNet Large Scale Visual Recognition Challenge. *International Journal of Computer Vision*, *115*(3), 211–252. https://doi.org/10.1007/s11263-015-0816-y

Salameh, C., Bard, P.-Y., Guillier, B., Harb, J., Cornou, C., Gérard, J., & Almakari, M. (2017). Using ambient vibration measurements for risk assessment at an urban scale: From numerical proof of concept to Beirut case study (Lebanon). *Earth, Planets and Space*, *69*(1), 60. https://doi.org/10.1186/s40623-017-0641-3

SESAME Project (2004). (s.d.). *Guidelines for the implementation of theH/V spectral ratio technique on ambient vibrations measurements, processing and interpretation*

Sgattoni, G., & Castellaro, S. (2020). Detecting 1-D and 2-D ground resonances with a single-station approach. *Geophysical Journal International*, *223*(1), 471–487. https://doi.org/10.1093/gji/ggaa325

Sgattoni G., Lattanzi G., Castellaro S., 2023. An experimental approach to unravel 2D ground resonances: application to an alluvial-sedimentary basin, *Earth, Planet and Space*, 75, 74

Tuan, T. T., Scherbaum, F., & Malischewsky, P. G. (2011). On the relationship of peaks and troughs of the ellipticity (H/V) of Rayleigh waves and the transmission response of single layer over half-space models: Relationship of peaks and troughs of H/V-ratio. *Geophysical Journal International*, *184*(2), 793–800. https://doi.org/10.1111/j.1365-246X.2010.04863.x

Van Der Baan, M. (2009). The origin of *SH* -wave resonance frequencies in sedimentary layers. *Geophysical Journal International*, *178*(3), 1587–1596. https://doi.org/10.1111/j.1365-246X.2009.04245.x

Vantassel, J.P., Stolte, A.C., Wotherspoon, L.M., Cox, B.R., 2023. AutoHVSR: A machine-learning-supported algorithm for the fully-automated processing of horizontal-to-vertical spectral ratio measurements. Soil Dyn. Earthq. Eng. 173, 108153. https://doi.org/10.1016/j.soildyn.2023.108153

Wang, P., Zimmaro, P., Ahdi, S. K., Yong, A., & Stewart, J. P. (2023). Identification Protocols for Horizontal-to-Vertical Spectral Ratio Peaks. *Bulletin of the Seismological Society of America*, *113*(2), 782–803. https://doi.org/10.1785/0120210304

Yaghmaei-Sabegh, S., & Tsang, H.-H. (2011). A new site classification approach based on neural networks. *Soil Dynamics and Earthquake Engineering*, *31*(7), 974–981. https://doi.org/10.1016/j.soildyn.2011.03.004

Yong, A., Martin, A., Stokoe, K., & Diehl, J. (2013). *ARRA-funded VS30 measurements using multi-technique approach at strong-motion stations in California and central-eastern United States*. U.S. Geological Survey.

Zhao, J. X. (2006). An Empirical Site-Classification Method for Strong-Motion Stations in Japan Using H/V Response Spectral Ratio. *Bulletin of the Seismological Society of America*, *96*(3), 914–925. https://doi.org/10.1785/0120050124

Mailing address:
miriana.didonato3@unibo.it
silvia.castellaro@unibo.it